Interfacial superconductivity achieved in parent $AEFe_2As_2$ (AE = Ca, Sr, Ba) by a simple and realistic annealing route

Shuyuan Huyan,[1,†,*] Yanfeng Lyu,[1,†] Hua Wang,[2,†] Liangzi Deng,[1] Zheng Wu,[1] Bing Lv,[3] Kui Zhao,[1] Fei Tian,[1] Guanhui Gao,[4] Rui-Zhe Liu,[1] Xiaojing Ma,[5] Zhongjia Tang,[5] Melissa Gooch,[1] Shuo Chen,[1] Zhifeng Ren,[1] Xiaofeng Qian,[2] and Ching-Wu Chu[1,6,*]

[1]*Department of Physics and Texas Center for Superconductivity, University of Houston, Houston, Texas 77204, United States*

[2]*Department of Materials Science and Engineering, Texas A&M University, College Station, Texas 77843, United States*

[3]*Department of Physics, University of Texas at Dallas, Richardson, TX, 75080, USA*

[4]*Department of Materials Science and NanoEngineering, Rice University, Houston, Texas 77005, United States*

[5]*Department of Chemistry and Texas Center for Superconductivity, University of Houston, Houston, Texas 77204, United States*

[6]*Lawrence Berkeley National Laboratory, Berkeley, California 94720, United States*

[†]*These authors contributed equally*

***Corresponding Authors:**

Shuyuan Huyan, Email: shuyuan.huyan@gmail.com;

Ching-Wu Chu, Email: cwchu@uh.edu.

ABSTRACT: Materials with interfaces often exhibit extraordinary phenomena exemplified by rich physics, such as high-temperature superconductivity and enhanced electronic correlations. However, demonstrations of confined interfaces to date have involved intensive effort and fortuity, and no simple path is consistently available. Here we report the achievement of interfacial superconductivity in the non-superconducting parent compounds $AEFe_2As_2$, where AE = Ca, Sr, or Ba, by simple subsequent annealing of the as-grown samples in an atmosphere of As, P, or Sb. Our results indicate that the superconductivity originates from electron transfer at the interface of the hybrid van der Waals heterostructures, consistent with the two-dimensional superconducting transition observed. The observations suggest a common origin of interfaces for the non-bulk superconductivity previously reported in the $AEFe_2As_2$ compound family and provide insight for the further exploration of interfacial superconductivity.

KEYWORDS: Interfacial superconductivity, $AEFe_2As_2$, Hybrid van der Waals heterostructures, Annealing process, Charge-transfer model

TOC GRAPHIC

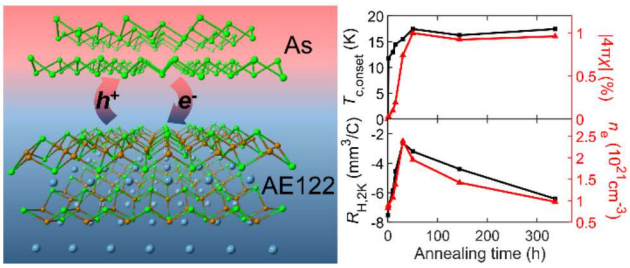
As
h+
e-
AE122
Tc,onset (K)
|4πχ| (%)
RH,2K (mm3/C)
ne (10-21cm-3)
Annealing time (h)

INTRODUCTION

Superconductivity has long been one of the most remarkable phenomena observed in condensed-matter physics. The search for superconductors with high transition temperatures (T_c), the development of potential applications for superconductors, and the unraveling of the pairing mechanism have continuously fueled the drive to find new material systems. With the advancement of experimental techniques, interfacial superconductivity in artificially assembled materials has attracted increasing interest in recent years. Superconductivity has been induced or enhanced in hybrid heterostructures at the interface between two materials, for example, ~3 K superconductivity in the mixture of Ru and Sr_2RuO_4,[1,2] ~0.2 K superconductivity in the $LaAlO_3/SrTiO_3$ heterostructure,[3,4] ~50 K superconductivity in the $La_{1.55}Sr_{0.45}CuO_4/La_2CuO_4$ heterostructure,[5] 65 K or even 109 K superconductivity in the monolayer FeSe films on $SrTiO_3$ substrates,[6,7] ~25 K superconductivity in the two-phase admixture of $CaFe_2As_2$,[8,9] and up to 1.7K superconductivity between two graphene layers twisted at a particular "magic" angle.[10] Such emergent superconductivity at interfaces resembles that of the reduced-dimension layered superconductors, such as cuprates,[11] iron-based superconductors,[12] and transition-metal dichalcogenide superconductors,[13,14] with very similar characteristics, thus providing ample opportunities to decode the pairing mechanisms of unconventional superconductors. Additionally, the capacity for nanometer- and even atomic-scale manipulation could benefit the search for high-T_c materials.

Superconductivity in the alkaline-earth iron arsenides $AEFe_2As_2$ (AE122, AE = Ca, Sr, or Ba) has attracted intense research activity over the last ten years. To date, the 122-type system has been the most investigated of the iron-based materials and is widely thought to capture the main traits of this compound family. Its parent compounds have a $ThCr_2Si_2$ structure with a reported non-superconducting antiferromagnetic ground state and sufficient conduction carriers.[15] Interestingly, some 122-type materials show unusual superconducting properties, such as filamentary superconductivity in rare-earth-doped Ca122,[16–19] and what is more interesting is that even the parent compounds occasionally show non-bulk superconducting properties under ambient pressure.[8,20–25] Although superconductivity in AE122 has been extensively studied and various underlying mechanisms have been proposed, direct evidence for its origin remains elusive.

Here we report a comprehensive study, including magnetic, transport, and Hall measurements followed by theoretical analyses, on the parent AE122 compounds annealed in the atmosphere of different elements: P, As, Sb, Se, or Te. Our results show that superconductivity emerges in the AE122 samples after annealing with As, P, or Sb, while no superconductivity was observed for those with Se or Te. Through systematic experiments and analyses of Ca122 annealed with As, as an example, we found that the superconductivity undergoes a Berezinskii-Kosterlitz-Thouless (BKT)-like transition[26] and is located at the surface of the Ca122 sample. Hall measurements suggest that the observed superconductivity is induced by electron doping resulting from the interfaces that appear after annealing and can be rationally explained by a phenomenological charge-transfer model consistent with density functional theory (DFT) calculations based on an

As/Ca122 van der Waals (vdW) heterostructure. The present study on the interface-induced superconductivity in these heterostructures offers valuable insights into the unusual occurrence of superconductivity in the AE122 compound system.

SUPERCONDUCTIVITY IN Ca122 ANNEALED WITH As

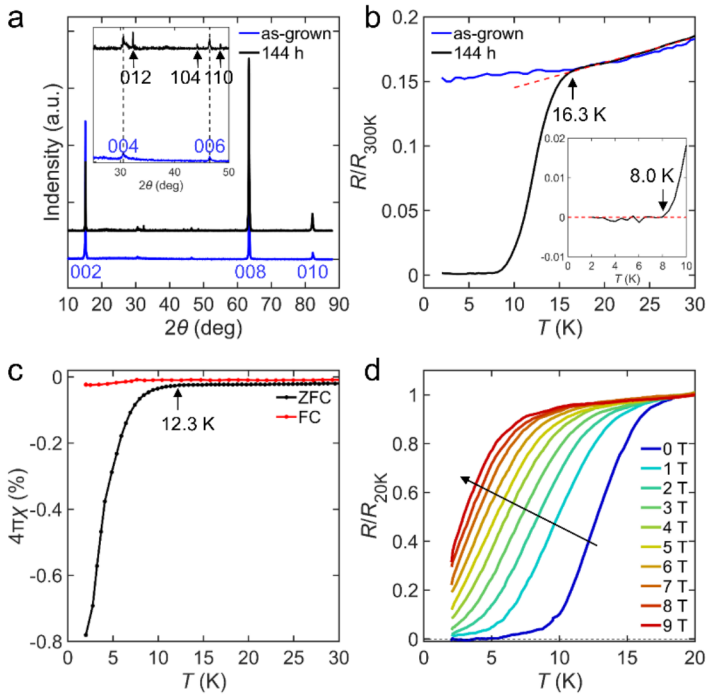

Figure 1. Ca122-As sample characterizations. (a) XRD spectra of as-grown Ca122 and Ca122-As annealed for 144 h, denoted by blue and black curves, respectively. Inset: magnified view to show the peaks from grey As. (b) Normalized $R(T)$ of the two samples at zero magnetic field. The Ca122-As sample shows a superconducting transition at $T_{c,onset} = 16.3$ K and $T_{c,zero} = 8$ K. Inset: magnified view of the zero-resistance state in 144-h Ca122-As. (c) ZFC and FC magnetization of the Ca122-As sample measured in a field of 5 Oe. The Meissner screening volume fraction is about 1%. (d) Variation of $R(T)$ of the Ca122-As sample in magnetic fields of 0-9 T perpendicular to the sample plane.

Figure 1a shows the X-ray diffraction (XRD) patterns of as-grown Ca122 and Ca122 annealed with elemental As (Ca122-As). Here we denote the starting sample before further annealing under an As atmosphere as the as-grown sample. Details of the sample preparation and the subsequent annealing process are provided in the Materials and methods section in the Supporting Information and Figure S1. The as-grown Ca122 sample has a tetragonal phase at room temperature and ambient pressure (blue curve in Figure 1a). Low-temperature XRD spectra of as-grown Ca122 focused on the (008) peak (Figure S2a) clearly show that the sample undergoes a tetragonal-to-orthorhombic phase transition between 150 K and 170 K, which is characteristic of the PII phase according to previous reports.[8,9,27–30] After measurements of the as-grown Ca122 samples were completed, they were annealed at 350 °C under an As atmosphere for different amounts of time. The XRD profile of the 144-hour (144-h) Ca122-As sample (black curves in Figure 1a and its inset)

shows extra peaks when compared with that of the as-grown sample, which is attributable to grey arsenic. Besides Ca122 and As, no additional peaks were detected, which indicates that there are no evident chemical reactions between Ca122 and As at the annealing temperature studied. On the other hand, when Ca122-As samples were annealed for shorter amounts of time, no extra As diffraction peaks were observed, likely due to a smaller amount of As deposited on the Ca122 surface. Furthermore, the surface color of the 144-h annealed sample is distinctly different from that of the as-grown sample. The chemical composition of different layers in this annealed sample was verified by energy-dispersive X-ray spectroscopy (EDS), as shown in Figure S3, which verifies that the excess As exists exclusively on the surface as expected, and that the inner layers are almost stoichiometric.

Interestingly, superconductivity emerges in the Ca122-As samples, as shown by electrical and magnetic transport measurements as functions of temperature, which are described in detail below. The temperature-dependent electrical resistance (R) at zero applied magnetic field of the as-grown Ca122 and 144-h Ca122-As samples is shown in Figure 1b. The R (T) /$R_{300\ K}$ curves of both samples show a first-order phase transition at $T_N \sim 170$ K (Figure S2b,c) corresponding to the paramagnetic tetragonal-to-antiferromagnetic orthorhombic phase transition. The T_N shows no significant change after subsequent annealing with As, indicating that the interior of the Ca122-As sample remains intact. As the temperature is further lowered, the Ca122-As sample exhibits a superconducting transition at $T_{c,onset} \sim 16.3$ K, and a zero-resistance transition occurs at $T_{c,zero} = 8$ K. The resistance drops steeply to zero below the noise limit of our measurement (inset, Figure 1b). The transition width is rather broad, suggesting the inhomogeneous distribution of superconductivity in the sample. The zero-field-cooled (ZFC) and field-cooled (FC) *dc* susceptibilities of the Ca122-As sample at magnetic field $H = 5$ Oe (Figure 1c) show a substantial drop, indicating that the onset of transition appears at ~12.3 K, which is between its $T_{c,onset}$ and $T_{c,zero}$. The shielding volume fraction estimated from the ZFC measurement is less than 1%, indicating the non-bulk nature of its superconductivity. Figure 1d displays $R(T)/R_{20K}$ curves of the Ca122-As sample measured at different magnetic fields perpendicular to the sample plane and shows that the $T_{c,onset}$ and $T_{c,zero}$ are clearly suppressed by magnetic fields. The occurrence of the zero-resistance state and it characteristic $R(T,H)$ dependence provide clear evidence for superconductivity in the Ca122-As sample.

The superconductivity in the Ca122-As samples is very sensitive to annealing time. As shown by the triangles in Figure 2a, $T_{c,onset}$ increases from 10 K to 17 K with increasing annealing time between 1 hour (1 h) and 50 h and remains almost unchanged with even longer annealing time. The zero-resistance state is observed in Ca122-As samples with annealing time of 50 h to 336 h, but the $T_{c,zero}$ decreases with increasing time within this range. Correspondingly, the superconducting shielding fraction estimated by ZFC at 2 K (Figure 2b) increases with increasing annealing time up to 50 h and tends to saturate above a critical time. The upper panel of Figure 2d clearly summarizes the evolution of the $T_{c,onset}$ from $R(T)$ and the $4\pi\chi$(2 K) with annealing time.

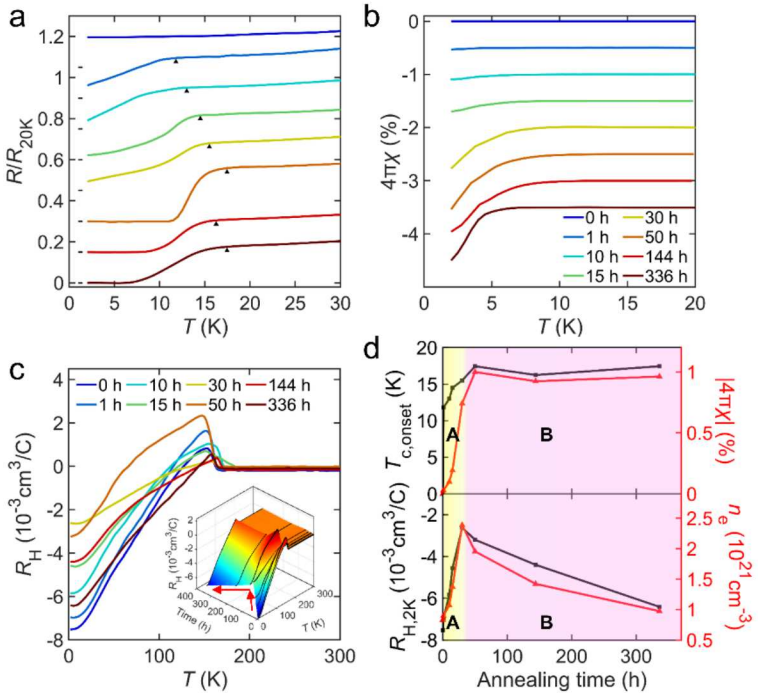

Figure 2. Superconductivity as a function of annealing time. (a−c) $R(T)$, $4\pi\chi(T)$, and $R_H(T)$ curves of Ca122-As, respectively, for different amounts of annealing time. The inset to (c) is a 3D plot clearly indicating the R_H evolution as a function of annealing time. (d) Upper panel: annealing-time-dependent $T_{c,onset}$ from $R(T)$ and Meissner screening volume fraction at 2 K for Ca122-As; lower panel: annealing-time-dependent R_H and n_e of Ca122-As.

The corresponding Hall coefficient (R_H) results, reflecting the global (bulk and surface) carriers in the samples, indicate a systematic evolution with respect to annealing time, as shown in Figure 2c. The as-grown Ca122 sample shows a typical behavior similar to that previously reported.[29] Despite the sizable systematic error, the R_H (2 K) (lower panel, Figure 2d) reveals two distinct annealing time regions. R_H first monotonically increases with increasing annealing time ranging from 1 h to 30 h, and then decreases with further increasing annealing time from 50 h to 336 h without saturation. Based on these time-dependent R_H results, the time range for the annealing process can be respectively divided into an electron-carrier-increasing (e-injection) region A and an electron-carrier decreasing (e-rejection) region B (Figure 2d). The variation of $T_{c,onset}$ with annealing time correlates well with that for R_H. The above results indicate that the annealing process initially injects more electronic carriers into the system and induces superconductivity. The effective density of carriers (n_e) reaches a maximum at an annealing time of between 30 h and 50 h in region A, and then decreases with further increasing annealing time due to the more pronounced effect of the e-rejection channels in region B, as shown in the lower panel of Figure 2d. However, the T_c exhibits little change in region B. The non-monotonic behavior or T_c dependence of the e-injection and the T_c independence of the e-rejection indicate that the e-injection and e-rejection processes occur at different locations in the samples and that superconductivity is triggered only in a particular area of the Ca122 samples with injected

electrons, resulting in the very low volume fraction found in this system. All of these observations can be well explained in terms of interfacial superconductivity when the influences introduced by annealing in an As atmosphere are taken into consideration, as discussed below.

There are three possibilities for Ca122 single-crystal samples annealed in an As atmosphere at 350 °C: (1) As intercalation into Ca122 layers, Fe-site vacancies, or As substitution during annealing; (2) formation of amorphous As on the Ca122 sample surface during the cooling process after annealing; and (3) formation of crystalline As on the Ca122 sample surface during annealing. The possibility of either Fe-site vacancies or As substitution is low because the annealing temperature is much lower than the decomposition temperature of Ca122. Among the options in possibility (1), only As intercalation into the Ca122 layers is able to occur, and according to the electronegativity of As, As intercalation usually serves as a hole-doping dopant, which coincidently corresponds to region B of decreasing n_e shown in Figure 2d. During the cooling process after annealing, possibility (2) might occur when the temperature is lower than the 250 °C crystallization temperature of As.[31,32] However, the cooling procedure for every annealing case is identical, so this effect is unable to cause systematic changes in physical properties. Possibility (3) is very likely to occur because the crystallization temperature of As is within the annealing temperature range,[31,32] and no extra energy is needed for diffusion into the Ca122 single crystal below its surface, in comparison with the options in possibility (1). In addition, we conducted a comparative experiment in which we placed the as-grown Ca122 sample at the cool-zone side of the quartz tube during the subsequent annealing process, in contrast to the procedure described in the Materials and methods section in the Supporting Information section and Figure S1, and further cooled the cool zone using dry ice. The resulting samples have only uncrystallized As on the surface, so possibility (3) does not occur and the samples do not exhibit superconductivity (Figure S4a). Taking into consideration the relatively low crystallization temperature of As, we preserved these samples in a glove box filled with argon gas at room temperature for tens of weeks. The uncrystallized As might recrystallize again along the Ca122 lattice during long-term storage. As expected, these stored samples do show trace superconductivity (Figure S4b), indicating the crucial role of As crystallization on the surface. Thus, among the three possibilities described above, possibility (3) is the most plausible one to explain the superconductivity observed here, showing that it is novel interfacial superconductivity, which will be described below.[33]

INTERFACIAL CHARACTERISTIC OF SUPERCONDUCTIVITY IN Ca122 ANNEALED WITH As

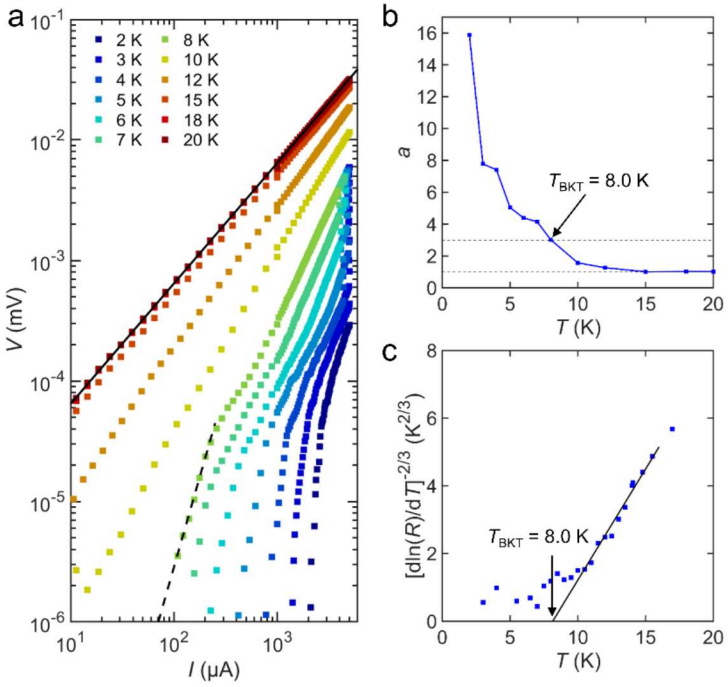

Figure 3. $V(I)$ characteristics of the 144-h Ca122-As sample showing the BKT transition. (a) Temperature-dependent $V(I)$ curves on a logarithmic scale. The black solid lines are fits of the data at the transition. The short black dashed line corresponds to $V \sim I^3$ dependence. (b) Temperature dependence of the power-law exponent a, as deduced by fitting from (a). (c) $R(T)$ dependence, plotted on a $[\mathrm{dln}(R)/\mathrm{d}T]^{-2/3}$ scale. The black solid line denotes the behavior expected for a BKT transition with $T_{\mathrm{BKT}} = 8.0$ K.

The BKT transition has been reported in neutral superfluids.[34] In principle, the BKT model is not expected to occur in infinitely large thin superconducting films[35] because the interaction between the Pearl vortices[36] falls off as $1/r$ rather than $\ln(r)$ at long distances, which implies that isolated vortices have a finite energy and can be thermally excited at all temperatures. However, for a sufficiently thin and dirty superconducting film that has a sample size smaller than the effective (Pearl) penetration depth $\lambda_{eff}^{(2D)}$, the analogy to the case of a neutral superfluid is essentially exact.[26] The BKT transition has been observed in ultra-thin superconducting films, especially interfacial superconductors.[37–40] In our case, if the 144-h Ca122-As sample is a two-dimensional (2D) superconductor, its superconducting transition can exhibit a BKT-like transition, characterized by a transition temperature T_{BKT} at which vortex-antivortex pairs unbind. Figure 3a displays the dc voltage *vs.* current (*V-I*) characteristics of the sample from 2 to 20 K at zero field. The 144-h Ca122-As sample indeed shows clear signatures of BKT behavior, such as $V \propto I^a$ power-law dependence, with systematic change in the exponent a consistent with that expected theoretically for the BKT transition. As shown in Figure 3b, a deviates from 1 and approaches 3 at $T = 8$ K, which is identified as T_{BKT}.[41] This value is the same as the sample's $T_{\mathrm{c,zero}}$ (Figure 1b). Additionally, the observed $R(T)$ characteristics are consistent with a BKT-like transition, *i.e.*, close to T_{BKT}, $R(T)=R_0\exp[-b(T/T_{\mathrm{BKT}}-1)^{1/2}]$, where R and b are material-dependent parameters. As shown in Figure 3c, the $[\mathrm{dln}(R)/\mathrm{d}T]^{-2/3}$ *vs.* T curve yields $T_{\mathrm{BKT}} = 8$ K, which is consistent with the results of

the *V-I* analysis. Some theoretical studies have shown that the size effect may still destroy the BKT transition even if the samples are made small enough.[42,43] To further test the BKT behavior in future studies, it will be worth conducting additional measurements, such as the high frequency measurement.[44–46]

Furthermore, the zero-resistance state observed in $R(T)$ measurements of the 336-h annealed sample no longer appears after gently scratching in the middle of both top and bottom surfaces of the sample (Figure S5), indicating that the superconducting pathway was cut off. Figure S5 also shows that the superconductivity was almost destroyed after the further removal of very thin top layers on both sides of the sample. The experiments indicate that the < 1% superconductivity indeed only exists on the surface. Additionally, we carried out analyses of the upper critical fields under magnetic fields up to 9 T for $H//c$ and $H//ab$, the behavior of which also indicates the 2D-like characteristic of the superconductivity (Supplementary Section 6).

SUPERCONDUCTIVITY ACHIEVED IN AE122 BY A SIMPLE AND REALISTIC ROUTE

More interestingly, superconductivity is achieved not only in Ca122-As but also in Ca122-P and Ca122-Sb samples with different optimized $T_{c,onset}$ values of about 12.5 K and 7 K, respectively. On the other hand, Ca122-Se and Ca122-Te samples show no superconductivity down to 2 K (Figure 4a,b). Determining the reason for this abnormality would solve the mystery of superconductivity in this compound system and provide a simple route to achieve superconductivity in the AE122 parent compound.

As a contrasting experiment, Ca122 samples were systematically annealed with Se for different time periods using the same procedure as that for Ca122-As, and their R_H and n_e values are shown in Figure 4d,e, using the same analysis protocol as for Ca122-As (Figure 2d). Distinctly, the n_e of Ca122-Se monotonically decreases with increasing annealing time without showing the increase denoted as region A in Fig 2d, and Ca122-Se also exhibits semiconducting behavior (Figure S7). Additionally, the rapid decline of n_e with increasing annealing time up to 30 h shows that annealing with Se only has the e-rejection effect on Ca122 at the interface. Comparing the behaviors of Ca122-As and Ca122-Se allows us to conclude that e-injection plays a role in realizing superconductivity in Ca122. The different effects of annealing with As and Se prompt us to consider their different work function (Φ) values.[47] The relationship between the optimized $T_{c,onset}$ values of Ca122 annealed with different elements and the Φ values of these elements is summarized in Figure 4c, which shows a nearly linear inverse relationship and indicates that the superconducting carrier density depends on the difference in Φ values between Ca122 and the annealing element, which causes Fermi level alignment and charge transfer.

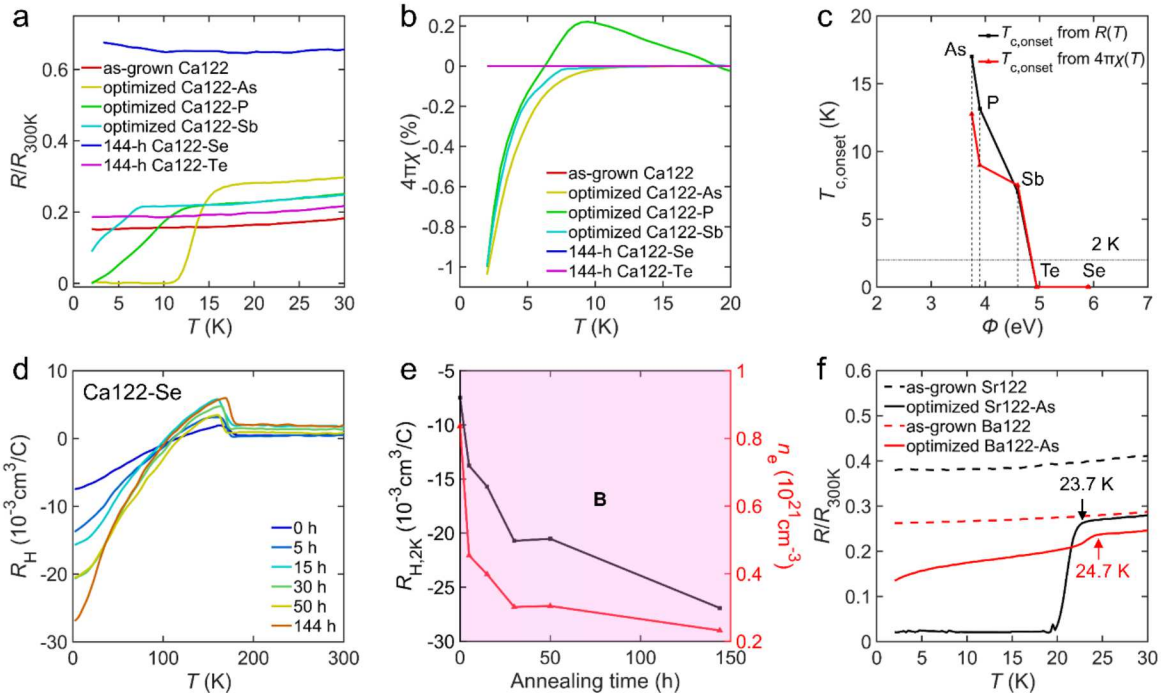

Figure 4. Observations of superconductivity in Ca122-P and Ca122-Sb and in other AE122 materials. (a,b) $R(T)$ and $4\pi\chi(T)$ of Ca122 annealed with P and Sb under optimized annealing conditions, and with Se and Te for 144 h. (c) The optimized $T_{c,onset}$ of Ca122 annealed with different elements measured from $R(T)$ and $4\pi\chi(T)$ as a function of the elements' work function Φ. (d) $R_H(T)$ of Ca122-Se. (e) Annealing-time-dependent $R_H(T)$ and n_e of Ca122-Se. In contrast to Ca122-As shown in Figure 2d, Ca122-Se exhibits only region B behavior. (f) $R(T)$ of Ba122 and Sr122 annealed with As under optimized annealing conditions (solid curves). The as-grown samples are shown as dashed curves.

More generally, we observed superconductivity in Sr122 and Ba122 (Figure 4f) by annealing them with As, and their optimized $T_{c,onset}$ values are around 23.7 K and 24.7 K, respectively, which are very close to those previously reported.[23–25] We did not observe the Meissner effect in Ba122-As (Figure S8), which is consistent with a previous report on Ba122.[25] The consistency between our findings and those of others suggest a common interpretation of sporadic observations of superconductivity in AE122 parent compounds: during the single-crystal synthesis, if some residual As remains in the reacting batch, sintering with this As could assist the emergence of superconductivity in AE122 as we observed in the current study.

PHENOMENOLOGICAL MODEL AND THEORETICAL ANALYSIS

Here we provide a simple phenomenological model for Ca122-As and Ca122-Se before and after

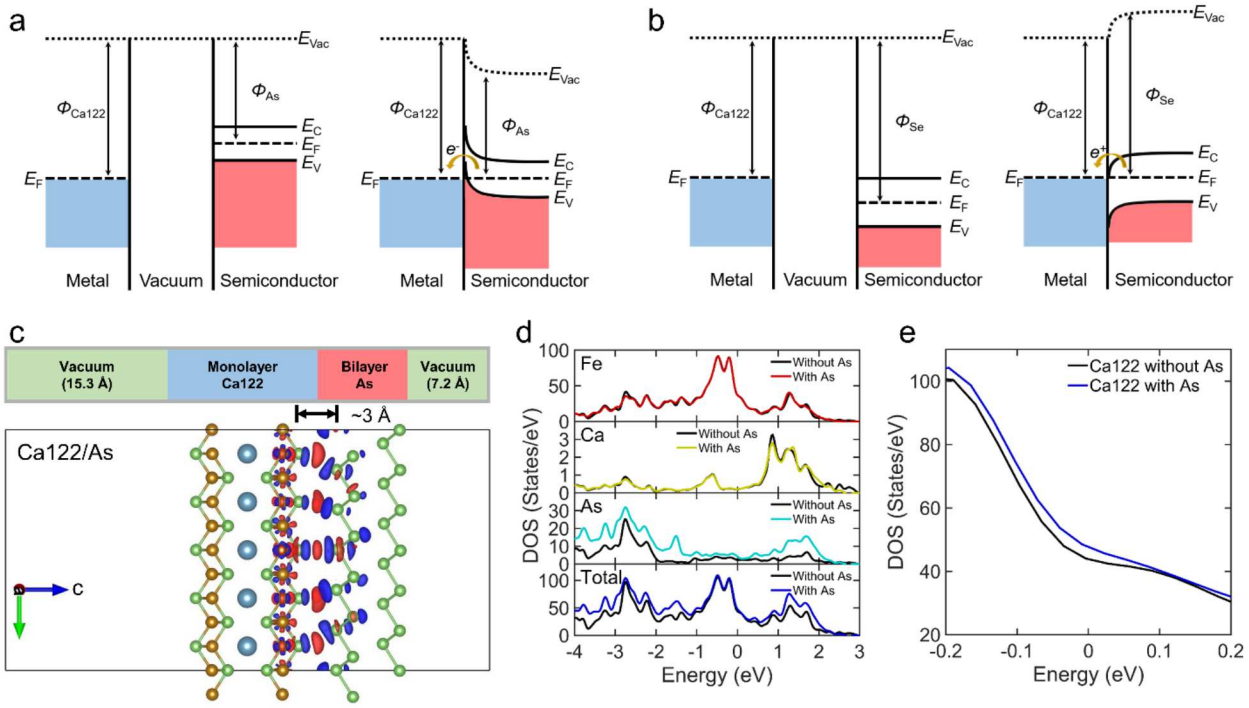

Figure 5. Phenomenological model and DFT calculations. (a,b) Energy-band-bending diagrams of interfaces between Ca122 and As (a) or Se (b), the work function (Φ) of which is respectively lower or higher than that of Ca122 with the As layer as the termination. (c) Charge accumulation (red regions) and depletion (blue regions) upon the stacking of bilayer As on the monolayer Ca122 structure. (d) Total DOS and projected DOS of Fe, Ca, and As from first-principles calculations for monolayer Ca122 without and with bilayer As atop. (e) Magnified view of the total DOS around the Fermi level.

contact (Figure 5a,b, respectively) to understand the novel superconductivity in Ca122 based on the charge-transfer mechanism. Ca122-As and Ca122-Se are simply treated as metal-semiconductor junctions because Ca122 and Se are a metal and a semiconductor, respectively; although As is generally a semimetal, it undergoes a semimetal-to-semiconductor transition when the thickness of the As layer is less than 40 nm.[48] On the other hand, since the as-grown Ca122 samples were cleaved at room temperature and in Ar gas before subsequent annealing and the alkaline earth metals have very strong reactivity, with suppression of their surface ordering as terminations, we assume As-termination to be the outer layer of Ca122, and its work function (Φ) is around 5.0 eV.[49] Due to the difference in Φ, the Fermi level alignment of the two sides induces band bending and charge transfer across the interface. Electrons are pushed to the Ca122 side in the case of Ca122-As, while holes are pushed to the Ca122 side in the case of Ca122-Se, which explains perfectly the observations of electron-doping-like behavior in Ca122-As and hole-doping-like behavior in Ca122-Se. Due to the competition of possibility (1) for Ca122 annealed in an As atmosphere as discussed above, as well as the electron-transfer mechanism and saturation of electron transfer after full coverage of As during long-term annealing, the n_e of Ca122-As changes from increasing to decreasing with increasing annealing time, while that for Ca122-Se only shows a decreasing trend with increasing annealing time.

To address the interfacial charge-transfer mechanism more concretely, we carried out a first-principles DFT calculation for a simple model of bilayer As on monolayer Ca122. The pristine lattice parameters and geometries of the As/Ca122 supercell structure were optimized. After the structural full relaxation, the As atoms only possess a very small lattice mismatch with the Ca122, demonstrating the harmonization of the supercell. Charge density difference maps, as plotted in Figure 5c, qualitatively elucidate the charge transfer status of the supercell. At the interface, the red regions represent charge accumulation while the blue regions represent charge depletion. The distribution of charge density indicates that the most significant charge transfer happens between the first As monolayer As and the first FeAs triple layer, while the second As monolayer, the second FeAs triple layer, and the underlying Ca layer are relatively unaffected, implying the very strong charge distribution between the nearest composites. The DFT-simulated density-of-states (DOS) spectrum is also generally consistent with our expectation, as shown in Figure 5d,e.

For further verification of the charge-transfer mechanism, we also performed a quantitative Bader charge analysis based on DFT calculations. The calculated Bader charge of As layers with and without Ca122 is shown in Table S1. Considering an effective thickness of 1 nm, the total charge transferred is ~3.3×10^{20} cm^{-3}, which roughly falls into the range from ~3.5×10^{19} to ~7.8×10^{20} cm^{-3} as estimated by Hall measurements (here we considered that there are two As/Ca122 interfaces in the Ca122-As sample since it has two large surfaces). The constitution of this heterostructure is of the vdW type and does not require a lattice match to obtain the proper bond alignment, which benefits the flexibility and achievability of the heterostructure. The small vdW distance, ~3 Å here, enables interface hybridization and charge transfer. On the other hand, the lone pairs outside the As atomic plane, which are not shared with other atoms in covalent bonds, will much more easily enhance the charge transfer by wavefunction overlap.

OUTLOOK

By applying a simple annealing method, we have unambiguously achieved superconductivity in parent AE122 compounds, where AE = Ca, Sr, or Ba. The superconductivity is characterized by 2D-like properties and is explained by a phenomenological charge-transfer mechanism and numerical simulation. The mechanism underlying the realization of superconductivity in AE122 provides a possible interpretation for intriguing reports of superconductivity in AE122 systems. The engineering of the vdW heterostructure offers a highly practical approach for further exploration of new superconductors and enables unique opportunities to investigate the many-body phase diagram as a direct function of interaction strength. Our study also provides a chance to study the moiré pattern, which is introduced either by lattice mismatch or rotational misalignment and results in a long wavelength superlattice. Under proper circumstances, the resulting superlattice miniband can become exceptionally flat, causing correlation physics to observably manifest by the emergence of a new ground state at partial band filling.

ASSOCIATED CONTENT

Supporting Information

SI provides a description of materials and methods, a schematic setup for annealing, temperature-dependent XRD spectra, chemical composition evolution from SEM measurement, comparative dry-ice-procedure experiment, $R(T)$ measurement after surface destruction, upper critical field analyses, metal-insulator transition behavior of Ca122-Se, magnetic susceptibility of Sr122-As and Ba122-As, and Bader charge calculation for the model of bilayer As on monolayer Ca122.

AUTHOR INFORMATION

Corresponding Authors

Shuyuan Huyan − *Department of Physics and Texas Center for Superconductivity, University of Houston, Houston, Texas 77204, United States;*

Email: shuyuan.huyan@gmail.com

Ching-Wu Chu – *Department of Physics and Texas Center for Superconductivity, University of Houston, Houston, Texas 77204, United States; Lawrence Berkeley National Laboratory, Berkeley, California 94720, United States;*

Email: cwchu@uh.edu.

Authors

Yanfeng Lyu − *Department of Physics and Texas Center for Superconductivity, University of Houston, Houston, Texas 77204, United States*

Hua Wang − *Department of Materials Science and Engineering, Texas A&M University, College Station, Texas 77843, United States*

Liangzi Deng − *Department of Physics and Texas Center for Superconductivity, University of Houston, Houston, Texas 77204, United States*

Zheng Wu − *Department of Physics and Texas Center for Superconductivity, University of Houston, Houston, Texas 77204, United States*

Bing Lv − *Department of Physics, University of Texas at Dallas, Richardson, TX 75080, USA;*

Kui Zhao − *Department of Physics and Texas Center for Superconductivity, University of Houston, Houston, Texas 77204, United States*

Fei Tian − *Department of Physics and Texas Center for Superconductivity, University of Houston, Houston, Texas 77204, United States*

Guanhui Gao − *Department of Materials Science and NanoEngineering, Rice University, Houston, Texas 77005, United States*

Rui-Zhe Liu − *Department of Physics and Texas Center for Superconductivity, University of Houston, Houston, Texas 77204, United States*

Xiaojing Ma − *Department of Chemistry and Texas Center for Superconductivity, University of Houston, Houston, Texas 77204, United States*

Zhongjia Tang− *Department of Chemistry and Texas Center for Superconductivity, University of Houston, Houston, Texas 77204, United States*

Melissa Gooch − *Department of Physics and Texas Center for Superconductivity, University of Houston, Houston, Texas 77204, United States*

Shuo Chen − *Department of Physics and Texas Center for Superconductivity, University of Houston, Houston, Texas 77204, United States*

Zhifeng Ren − *Department of Physics and Texas Center for Superconductivity, University of Houston, Houston, Texas 77204, United States*

Xiaofeng Qian − *Department of Materials Science and Engineering, Texas A&M University, College Station, Texas 77843, United States*

Author Contributions

S.H., Y.L., Z.W., and C.-W.C. designed and coordinated the experiments. S.H., Z.W., B.L., F.T., R.L., Z.T., and Z.R. contributed to the sample preparation. S.H., Y.L., L.D., and Z.W. carried out the XRD, SEM, EDS, electrical, and magnetic transport measurements. H.W. and X.Q. carried out the DFT calculations. S.H., Y.L., K.Z., G.G., X.M., M.G., and S.C. contributed to discussions about the data. S.H., Y.L., H.W. and C.-W.C. wrote the manuscript with contributions from all of the authors.

S.H., Y.L., and H.W. contributed equally to this work.

Notes

The authors declare no competing financial interest.

ACKNOWLEDGMENTS

The work performed at TcSUH is supported in part by US Air Force Office of Scientific Research (AFOSR) Grants FA9550-15-1-0236 and FA9550-20-1-0068, the T. L. L. Temple Foundation, the John J. and Rebecca Moores Endowment, and the State of Texas through the Texas Center for Superconductivity at the University of Houston. X.Q. acknowledges support by the National Science Foundation under award number DMR-1753054. H.W. gratefully acknowledges support from the Texas A&M University President's Excellence Fund X-Grants and T3 Program. Z.R. acknowledges support by the Office of Naval Research under MURI Grant N00014-16-1-2436. The work at UT Dallas is partially supported by AFOSR Grant FA 9550-19-1-0037. We thank Chin-Sen Ting, Sheng Ran, and Hua Guo for helpful discussions and technical support.

REFERENCES

(1) Maeno, Y. et al. Enhancement of superconductivity of Sr_2RuO_4 to 3 K by embedded metallic microdomains. *Phys. Rev. Lett.* **81**, 3765–3768 (1998).

(2) Yaguchi, H., Wada, M., Akima, T., Maeno, Y. & Ishiguro, T. Interface superconductivity in the eutectic Sr_2RuO_4−Ru: 3-K phase of Sr_2RuO_4. *Phys. Rev. B* **67**, 214519 (2003).

(3) Ohtomo, A. & Hwang, H. Y. A high-mobility electron gas at the $LaAlO_3/SrTiO_3$ heterointerface. *Nature* **427**, 423–426 (2004).

(4) Reyren, N. et al. Superconducting interfaces between insulating oxides. *Science* **317**, 1196–1199 (2007).

(5) Gozar, A. et al. High-temperature interface superconductivity between metallic and insulating copper oxides. *Nature* **455**, 782–785 (2008).

(6) Wang, Q. Y. et al. Interface induced high temperature superconductivity in single unit-cell FeSe films on $SrTiO_3$. *Chin. Phys. Lett*. **29**, 037402 (2012).

(7) Ge, J.-F. et al. Superconductivity above 100 K in single-layer FeSe films on doped $SrTiO_3$. *Nat. Mater.* **14**, 285–289 (2015).

(8) Zhao, K. et al. Interface-induced superconductivity at ~25 K at ambient pressure in undoped $CaFe_2As_2$ single crystals. *Proc. Natl Acad. Sci. U.S.A.* **113**, 12968–12973 (2016).

(9) Huyan, S. et al. Low-temperature microstructural studies on superconducting $CaFe_2As_2$. *Sci. Rep.* **9**, 6393 (2019).

(10) Cao, Y. et al. Unconventional superconductivity in magic-angle graphene superlattices. *Nature* **556**, 43–50 (2018).

(11) Bednorz, J. G. & Müller, K. A. Possible high T_c superconductivity in the Ba−La−Cu−O system. *Z. Phys. B: Condens. Matter* **64**, 189−193 (1986).

(12) Kamihara, Y., Watanabe, T., Hirano, M. & Hosono, H. Iron-based layered superconductor $La[O_{1-x}F_x]FeAs$ (x = 0.05−0.12) with T_c = 26 K. *J. Am. Chem. Soc.* **130**, 3296−3297 (2008).

(13) Choi, W. et al. Recent development of two-dimensional transition metal dichalcogenides and their applications. *Mater. Today* **20**, 116−130 (2017).

(14) Manzeli, S., Ovchinnikov, D., Pasquier, D., Yazyev, O. V. & Kis, A. 2D transition metal dichalcogenides. *Nat. Rev. Mater.* **2**, 17033 (2017).

(15) Rotter, M. et al. Spin-density-wave anomaly at 140 K in the ternary iron arsenide $BaFe_2As_2$. *Phys. Rev. B* **78**, 020503 (2008).

(16) Rotter, M., Tegel, M. & Johrendt, D. Superconductivity at 38 K in the iron arsenide $(Ba_{1-x}K_x)Fe_2As_2$. *Phys. Rev. Lett.* **101**, 107006 (2008).

(17) Sasmal, K. et al. Superconducting Fe-based compounds $(A_{1-x}Sr_x)Fe_2As_2$ with A = K and Cs with transition temperatures up to 37 K. *Phys. Rev. Lett.* **101**, 107007 (2008).

(18) Lv, B. et al. Unusual superconducting state at 49 K in electron-doped $CaFe_2As_2$ at ambient pressure. *Proc. Natl. Acad. Sci. U.S.A.* **108**, 15705−15709 (2011).

(19) Deng, L. Z. et al. Evidence for defect-induced superconductivity up to 49 K in $(Ca_{1-x}R_x)Fe_2As_2$. *Phys. Rev. B* **93**, 054513 (2016).

(20) Xiao, H. et al. Evidence for filamentary superconductivity nucleated at antiphase domain

walls in antiferromagnetic $CaFe_2As_2$. *Phys. Rev. B* **85**, 024530 (2012).
(21) Chen, D.-Y. et al., Superconductivity in undoped $CaFe_2As_2$ single crystals. *Chin. Phys. Lett*. **33**, 067402 (2016).
(22) Wang, X. F. et al. Anisotropy in the electrical resistivity and susceptibility of superconducting $BaFe_2As_2$ single crystals. *Phys. Rev. Lett.* **102**, 117005 (2009).
(23) Tanatar, M. A. et al. Resistivity anisotropy of AFe_2As_2 (A = Ca, Sr, Ba): Direct versus Montgomery technique measurements. *Phys. Rev. B* **79**, 134528 (2009).
(24) Saha, S. R., Butch, N. P., Kirshenbaum, K., Paglione, J. & Zavalij, P. Y. Superconducting and ferromagnetic phases induced by lattice distortions in stoichiometric $SrFe_2As_2$ single crystals. *Phys. Rev. Lett*. **103**, 037005 (2009).
(25) Kim, J. S., Blasius, T. D., Kim, E. G. & Stewart, G. R. Superconductivity in undoped single crystals of $BaFe_2As_2$: field and current dependence. *J. Phys.: Condens. Matter* **21**, 342201 (2009).
(26) Beasley, M. R., Mooij, J. E. & Orlando, T. P. Possibility of vortex-antivortex pair dissociation in two-dimensional superconductors. *Phys. Rev. Lett*. **42**, 1165−1168 (1979).
(27) Ronning, F., Klimczuk, T., Bauer, E. D., Volz, H. & Thompson, J. D. Synthesis and properties of $CaFe_2As_2$ single crystals. *J. Phys.: Condens. Matter* **20**, 322201 (2008).
(28) Ran, S. et al. Stabilization of an ambient-pressure collapsed tetragonal phase in $CaFe_2As_2$ and tuning of the orthorhombic-antiferromagnetic transition temperature by over 70 K via control of nanoscale precipitates. *Phys. Rev. B* **83**, 144517 (2011).
(29) Saparov, B. et al. Complex structures of different $CaFe_2As_2$ samples. *Sci. Rep*. **4**, 4120 (2014).
(30) Gofryk, K. et al. Fermi-surface reconstruction and complex phase equilibria in $CaFe_2As_2$. *Phys. Rev. Lett*. **112**, 186401 (2014).
(31) Kochegarov, V. M. & Lomakina, T. P. An Investigation of the Kinetics of the Cathodic Deposition of Arsenic from Alkaline Solutions. *Sov. Electrochem*. **2**, 1120 (1966).
(32) Tammann, G. & Warrentrup, H. Korrosionsschutz des Eisens durch Arsen. *Z. Anorg. Allg. Chem.* **228**, 92–96 (1936).
(33) Miyata, Y., Nakayama, K., Sugawara, K., Sato, T. & Takahashi, T. High-temperature superconductivity in potassium-coated multilayer FeSe thin films. *Nat. Mater*. **14**, 775–779 (2015).
(34) Bishop, D. J. & Reppy, J. D. Study of the superfluid transition in two-dimensional ^{4}He films. *Phys. Rev. Lett.* **40**, 1727–1730 (1978).
(35) Kosterlitz, J. M. & Thouless, D. J. Long range order and metastability in two dimensional solids and superfluids. (Application of dislocation theory). *J. Phys. C: Solid State Phys.* **5**, L124–L126 (1972).
(36) Pearl, J. Current distribution in superconducting films carrying quantized fluxoids. *App. Phys. Lett.* **5**, 65–66 (1964).
(37) Hebard, A. F. & Fiory, A. T. Evidence for the Kosterlitz-Thouless transition in thin superconducting aluminum films. *Phys. Rev. Lett.* **44**, 291–294 (1980).

(38) Epstein, K., Goldman, A. M. & Kadin, A. M. Vortex-antivortex pair dissociation in two-dimensional superconductors. *Phys. Rev. Lett.* **47**, 534–537 (1981).
(39) Reyren, N. et al. Superconducting interfaces between insulating oxides. *Science* **317**, 1196–1199 (2007).
(40) Liu, C. et al. Two-dimensional superconductivity and anisotropic transport at $KTaO_3$ (111) interfaces. *Science* **371**, 716–721 (2021).
(41) Halperin, B. I. & Nelson, D. R. Resistive transition in superconducting films. *J. Low Temp. Phys.* **36**, 599–616 (1979).
(42) Kogan, V. G. Interaction of vortices in thin superconducting films and the Berezinskii-Kosterlitz-Thouless transition. *Phys. Rev. B* **75**, 064514 (2007).
(43) Gurevich, A. & Vinokur, V. M. Size effects in the nonlinear resistance and flux creep in a virtual Berezinskii-Kosterlitz-Thouless state of superconducting films. *Phys. Rev. Lett.* **100**, 227007 (2008).
(44) Minnhagen, P. Kosterlitz-Thouless transition for a two-dimensional superconductor: Magnetic-field dependence from a Coulomb-gas analogy. *Phys. Rev. B* **23**, 5745–5761 (1981).
(45) Minnhagen, P. The two-dimensional Coulomb gas, vortex unbinding, and superfluid-superconducting films. *Rev. Mod. Phys.* **59**, 1001–1066 (1987).
(46) Gasparov, V. A. et al. Magnetic field, frequency and temperature dependence of complex conductance of ultrathin $La_{1.65}Sr_{0.45}CuO_4/La_2CuO_4$ films and the organic superconductors κ-$(BEDT\text{-}TTF)_2Cu[N(CN)_2]Br$. *Int. J. Mod. Phys. B*, **29**, 1542012 (2015).
(47) Lide, D. R. CRC handbook of chemistry and physics. Taylor & Francis: London, 12–114 (2008).
(48) He, M. et al. Molecular-beam epitaxy growth of arsenic film and its semimetal-to-semiconductor transition. Appl. Phys. Lett. 83, 5452 (2003).
(49) Profeta, G., Franchini, C., Gamalath, K. A. I. L. W. & Continenza, A. First-principles investigation of $BaFe_2As_2$ (001). *Phys. Rev. B* **82**, 195407 (2010).